Dynamics of charge currents ballistically injected in GaAs by quantum interference

Hui Zhao,[1,a)] Eric J. Loren,[1] Arthur L. Smirl,[1,b)] and H. M. van Driel[2]
[1]*Laboratory for Photonics & Quantum Electronics, 138 IATL, University of Iowa Iowa City, Iowa 52242, USA*
[2]*Department of Physics and Institute for Optical Sciences, University of Toronto, Toronto M5S1A7, Canada*

(Received 28 June 2007; accepted 4 December 2007; published online 10 March 2008)

The dynamics of charge currents ballistically injected in GaAs bulk and quantum wells are spatially and temporally resolved. The electrons and holes are injected with oppositely directed velocities without the use of accelerating fields by quantum interference between two photon absorption of a 200 fs, 1430 nm fundamental pulse and one photon absorption of the corresponding second harmonic pulse. The subsequent charge motion is followed with ~200 fs temporal and ~1 nm spatial resolution by using tightly focused optical differential transmission techniques that are dependent on the relative phase of the incident pump pulses. Initially, the electrons and holes ballistically separate by up to ~20 nm, and a space charge field forms, which decelerates the carriers. Within this ~1 ps regime, the momentum relaxes by electron-hole and phonon scatterings, and the space charge field restores the electrons and holes to a common position; on time scales long compared to 1 ps, ambipolar diffusion and recombination complete the return of the system to equilibrium. A rigid shift (damped simple harmonic oscillator) model for the electron motion reproduces the key features in the data, and the procedure for extracting the spatiotemporal dynamics of the electrons is shown to be immune to energy relaxation effects and forgiving of nonlinear saturation. © *2008 American Institute of Physics*. [DOI: 10.1063/1.2840119]

I. INTRODUCTION

When an unbiased bulk semiconductor or multiple quantum well (MQW) is simultaneously irradiated with an optical pulse and its second harmonic, quantum interference between the two and one photon absorption pathways connecting the same initial and final states in the valence and conduction bands allows considerable control of the interband transitions.[1] For example, such two-color quantum interference and control (QUIC) processes can *ballistically* inject pure charge currents (without any net spin polarization),[2–9] pure spin currents (with no accompanying charge current),[9–12] and spin polarized currents.[13] These all-optical QUIC techniques have the advantage of being noninvasive, of not requiring the application of electrodes or the use of electric or magnetic fields, and of offering unprecedented control over the ballistic injection processes. The polarization states of the incident fields dictate the type of current (charge, spin, or both) that is injected, the polarization direction of the light establishes the direction of current flow, the phase of the light determines the magnitude and sign of the current, the frequency controls the magnitude of the initial ballistic velocity, and finally, the irradiance determines the carrier and current injection rates.

The ballistic transport associated with QUIC currents occurs over spatial scales comparable to the mean free path (a few nanometers) and is destroyed by momentum relaxation and modified by space charge fields on fs time scales. Previously, two-color QUIC currents have been detected by measuring the charge accumulation on electrodes,[3–5] by detecting the terahertz radiation emitted by the ballistic motion,[6] and by using optical pump-probe[7–9,11,13] and photoluminescence[12] techniques, but the charge and spin dynamics were not directly time resolved.

Recently, we have used tightly focused polarization-sensitive pump-probe techniques to follow the dynamics of ballistic pure *spin* currents injected into a GaAs quantum well by quantum interference between one-photon absorption of a linearly polarized second harmonic pulse and two photon absorption of an orthogonally polarized fundamental with ~1 nm spatial resolution and ~200 fs temporal resolution.[14] Because no net charge transport is associated with pure spin currents (i.e., equal numbers of spin-up electrons move in one direction and spin-down electrons in the other and the same for the holes), no dipole space charge fields are formed, and the carrier dynamics is particularly simple: spin-up and spin-down carrier profiles separate until momentum relaxation destroys the ballistic spin motion. The spin-up and spin-down profiles subsequently remain separated until they are destroyed by spin relaxation, diffusion, or recombination on much longer time scales. Here, we report the spatiotemporal resolution of pure *charge* currents injected by QUIC using fundamental and second harmonic pulses having the *same* parallel linear polarization. In contrast to pure spin currents, which cause spin separation, but no charge separation, pure charge currents produce charge separation, but no spin separation. We demonstrate that strong space charge fields are formed that strongly modify and complicate the charge dynamics.

[a)]Current address: Department of Physics and Astronomy, University of Kansas, Lawrence, KS 66045.
[b)]Electronic mail: art-smirl@uiowa.edu.

Also, with other colleagues,[15] we have previously demonstrated that a charge current *grating* can be injected in bulk GaAs at 300 K by the quantum interference between one and two photon absorption processes associated with *noncollinearly propagating* second harmonic and fundamental pulses. The onset and subsequent evolution of the electron charge, neutral population, and carrier temperature gratings established by the charge current grating were measured using the time resolved diffraction of a probe beam, which was resonant with continuum states. The growth and decay of the electron charge grating (and, consequently, the ballistic transport) could not be directly time resolved since its decay was found to be fast compared to the ~100 fs pump and probe pulse durations; however, its presence led to the formation of a temperature grating and a neutral population grating during the generation process. These temperature and population gratings dominated the resolvable dynamics.

By contrast, here, we focus on the direct temporal and spatial resolution of the change in electron position following ballistic injection by *collinearly propagating* tightly focused fundamental and second harmonic ~200 fs pulses on a GaAs sample at 80 K. Evolution of the electrons is determined by comparing the differential transmission (of a probe pulse tuned to the exciton line) that depends on the relative phase of the fundamental and second harmonic pump pulses to the differential transmission that is independent of that phase as a function of space and time. As discussed below, the procedure that we use to extract the distance that the electrons have moved and the time required for that movement is independent of carrier temperature and cooling, and it allows us to obtain information about the momentum scattering processes that destroy the ballistic transport and about the space charge fields that return the electrons and holes to a common position.

The organization of the paper is as follows. In Sec. II, we review the quantum interference process and describe the apparatus that is used to inject the pure charge currents. Section III qualitatively describes the charge dynamics following the ballistic injection, the apparatus for measuring the phase-independent and phase-dependent differential transmissions, and the procedure for extracting the electron position from the measurements. Section III also discusses and experimentally demonstrates that this procedure is independent of the relaxation in energy of the nonequilibrium carrier distribution (e.g., cooling). A simple rigid shift model for the electron motion that accounts semi-quantitatively for the measured features in the electron dynamics is presented in Sec. IV. Finally, in Sec. V, we demonstrate that the procedure for extracting the change in the electron position is forgiving of nonlinear saturation effects and verify that such effects do not measurable affect our results.

II. CURRENT INJECTION

Here, ballistic charge currents are injected by quantum interference when two copropagating, harmonically related pulses (with frequencies ω and 2ω) with the same parallel linear polarization (along $\hat{\boldsymbol{x}}$) are normally incident on the surface of a GaAs multiple quantum well grown along the

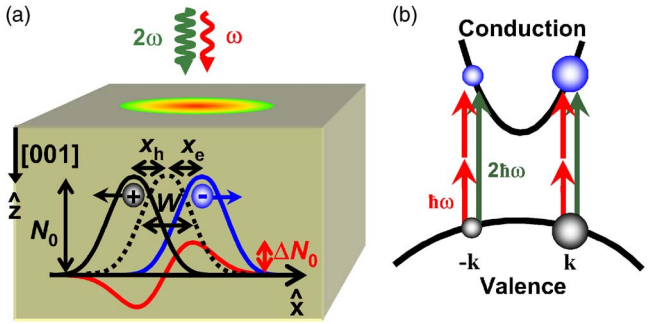

FIG. 1. (Color online) (a) Schematic showing the injection of charge current by colinearly polarized (along $\hat{\boldsymbol{x}}$) fundamental and second harmonic pump pulses with frequencies ω and 2ω, respectively. The electrons and holes are initially injected by two and one photon absorptions with an identical Gaussian spatial density profile (dashed curve of height N_0 and width W). For $\Delta\phi=\pi/2$, the electrons (holes) move to the right (left) with average velocity $\langle v_e\rangle$ ($\langle v_h\rangle$). As a result, the electrons (holes) travel a distance x_e (x_h) in time t, causing a peak differential change in electron density ΔN_0 (the corresponding differential change in hole density not shown for clarity). (b) Excitation scheme indicating that the quantum interference between the two and one photon absorptions of the ω and 2ω pump pulses, respectively, injects more carriers at $+k$ than at $-k$.

$\hat{z}=[001]$ direction, as shown schematically in Fig. 1(a). The complex electric fields of the incident pump pulses inside the crystal are written as

$$\boldsymbol{E}_{\omega}(\boldsymbol{r},t)=E_{\omega}(\boldsymbol{r},t)\hat{\boldsymbol{x}}\exp[i(-\omega t+k_{\omega}z+\phi_{\omega})], \tag{1}$$

$$\boldsymbol{E}_{2\omega}(\boldsymbol{r},t)=E_{2\omega}(\boldsymbol{r},t)\hat{\boldsymbol{x}}\exp[i(-2\omega t+k_{2\omega}z+\phi_{2\omega})], \tag{2}$$

where $E_{\omega,2\omega}$ are the electric field envelopes at position $\boldsymbol{r}$ and time t, and $k_{\omega,2\omega}$ and $\phi_{\omega,2\omega}$ are the propagation constants and phases, where ω is chosen such that $\hbar\omega<E_g<2\hbar\omega$ (E_g is the fundamental bandgap). As shown in Fig. 1(b), the ω and 2ω pump pulses connect the same initial and final states in the conduction and valence bands via two and one photon absorptions, respectively. Acting alone, each individual pulse excites a nonpolar distribution of carriers, i.e., equal numbers of electrons are excited at $+k$ and $-k$ states in the conduction band. Although each electron is injected with a ballistic speed on the order of 1000 km/s, the velocity of the electrons averaged over all k-space is zero, and consequently, there is no macroscopic current.

By comparison, when the two pulses are simultaneously present, the electron distribution injected by quantum interference between the transition amplitudes for one photon and two photon absorptions is polar, and more electrons are injected into states along one direction in k-space than along the other [Fig. 1(b)]. A current density is produced along $\hat{\boldsymbol{x}}$ at a rate given by[16,17]

$$\dot{J}_x=2|E_{\omega}|^2E_{2\omega}[\eta_{B1}+\eta_{B2}+\eta_C]\sin(\Delta\phi), \tag{3}$$

where $\Delta\phi=2\phi_{\omega}-\phi_{2\omega}$ and the *real* injection factors η_i $[i=B1,B2,C]$ are defined in terms of the three purely *imaginary*, nonzero elements of the third-order current injection tensor: $\eta_{B1}=-2i\eta_{aabb}$, $\eta_{B2}=-i\eta_{abba}$, and $\eta_C=2i\eta_{aabb}+i\eta_{abba}-i\eta_{aaaa}$, where a and b subscripts denote the crystallographic axes. Equation (3) also can be written phenomenologically as[1,3,7,17,18]

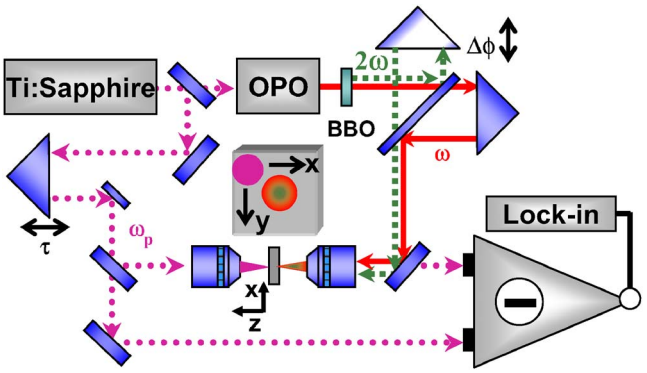

FIG. 2. (Color online) Experimental apparatus for injecting and spatially and temporally probing charge currents.

$$\dot{J}_x = e[\dot{N}_h\langle v_h\rangle - \dot{N}_e\langle v_e\rangle]\sin(\Delta\phi), \tag{4}$$

where e is the elementary charge, and $\dot{N}_e$ $(=\dot{N}_h)$ is the injection rate for electrons (holes) into the conduction (valence) band. The quantity $\langle v_e\rangle\sin(\Delta\phi)$ $[\langle v_h\rangle\sin(\Delta\phi)]$ is the average velocity of the electrons (holes) along the $\hat{x}$ direction,[17] and it can be viewed as reflecting the fraction of the injected electrons (holes) that participate in the charge current. As suggested in Figs. 1(a) and 1(b), electrons and holes are injected in the opposite directions with equal crystal momentum, and their contributions to the current add.

The experimental geometry for injecting these QUIC charge currents is shown in Fig. 2. The $\hat{x}$-polarized ω pulse is centered at 1430 nm and is obtained from a Ti:sapphire-pumped optical parametric oscillator (OPO) operating at 80 MHz. The 2ω pulse is generated by frequency doubling in a beta barium borate (BBO) crystal. The phase $\Delta\phi$ is controlled by a dichroic interferometer. Subsequently, the pulses are collinearly recombined and tightly focused at normal incidence onto the sample surface. The ω and 2ω pump profiles are spatially overlapped with an accuracy of $\sim$100 nm, and the focusing lens dispersively broadens each pulse to a width of $\sim$200 fs [full width at half maximum of the intensity (FWHM)].

The propagation sequence depicted in Fig. 2 (and described in the previous paragraph) automatically ensures that the single photon absorption of the 2ω pulse and the two photon absorption of the ω pulse produce Gaussian carrier density spatial profiles with the same diameter $W\sim 1.6$ μm (FWHM) [see dashed curve Fig. 1(a)]. This occurs in the following way. The second harmonic process in the BBO not only reduces the wavelength by a factor of 2 $(\lambda_{2\omega}=\lambda_\omega/2)$ but also decreases the diameter of the Gaussian spatial profile of the 2ω pulse by $\sqrt{2}$ compared to the fundamental ω beam (since $E_{2\omega}\propto E_\omega^2$). Because of its smaller wavelength, the beam with the narrower spatial profile (i.e., the 2ω pulse) is focused to the smaller spot on the sample. Specifically, the focused diameters at the sample are $\sim$1.6 and $\sqrt{2}\times 1.6$ μm (FWHM) for the 2ω and ω pulses, respectively. The carrier density profile generated by one photon absorption is proportional to the intensity of the 2ω pulse $(\propto I_{2\omega})$, and therefore, has the same width as $I_{2\omega}$, $\sim$1.6 μm. In contrast, the profile injected by two photon absorption is proportional to the square of the intensity of the ω pulse $(\propto I_\omega^2)$, and it has a width that is reduced by $\sqrt{2}$ compared to the focused diameter of I_ω, also $\sim$1.6 μm. In short, the second harmonic process intrinsically preconditions the ω pulse (in spatial profile) to guarantee that it will produce the same carrier profile by two photon absorption as the 2ω pulse produces by one photon absorption.

All measurements reported here are performed using a 40 period $GaAs/Al_{0.3}Ga_{0.7}As$ MQW structure with 10 nm wide wells (with band gap $E_g=1.533$ eV at 80 K) and 10 nm thick barriers, grown on a [001]-oriented GaAs substrate, but with the substrate removed following growth to allow transmission measurements. The propagation direction $\hat{z}$ for the pump pulses is carefully aligned along the [001] direction to avoid complications from charge or spin density control,[10,16,17] and the sample is oriented such that the laboratory coordinate axes, $\hat{x}$ and $\hat{y}$, coincide with the crystallographic axes, but these coordinate axes can be arbitrarily chosen since the charge currents are not strongly sensitive to the crystal orientation.[10,16,17] [For our orientation, the injection tensor in Eq. (3) simplifies to $\eta_{B1}+\eta_{B2}+\eta_C=-i\eta_{aaaa}$.] The center frequency of the 2ω pulse corresponds to an excess energy of $\sim$160 meV above the band edge and to an injection speed for each electron of $\sim$950 nm/ps. The electrons and holes are initially injected with the same Gaussian spatial density profile, $N_e(x,y,t=0)=N_h(x,y,t=0)$, with a peak density N_0 and spatial width W, as depicted by the dashed curve in Fig. 1(a).

There is no significance or advantage (other than the increased signal to noise that results from probing on the exciton) to the use of a MQW. We have also performed similar measurements on a 0.7 μm thick bulk sample and on two other $GaAs/Al_{0.3}Ga_{0.7}As$ MQW samples (a 10 period and a 20 period 14/14 nm MQW). While results show minor quantitative differences, the dynamics reported here are generic and representative.

III. CHARGE CURRENT SPATIOTEMPORAL DYNAMICS

Although the electrons and holes are initially injected with identical spatial profiles, they are injected with oppositely directed average ballistic velocities, $\langle v_e(t=0)\rangle\sin\Delta\phi$ and $\langle v_h(t=0)\rangle\sin\Delta\phi$, respectively, as indicated in Fig. 1(a). As a result, the electron and hole spatial distributions separate until the injected momentum relaxes by electron-hole and carrier-phonon scatterings. As the electrons and holes separate, a space charge field E_{sc} develops, which opposes the separation of the electrons and holes. Eventually, the restoring force associated with E_{sc} causes the electrons and holes to return to a common position. This motion is sketched in Fig. 3, assuming that the profiles shift rigidly.

The apparatus for monitoring the carrier motion also is shown in Fig. 2. A $\hat{y}$ polarized pulse at 803 nm is taken directly from the Ti:sapphire oscillator and is split into two parts: a probe pulse and a reference pulse. The probe pulse is tightly focused onto the sample by a lens identical to that used to focus the pump pulses. Consequently, the probe also is focused to a $W\sim 1.6$ μm (FWHM) diameter spot and is

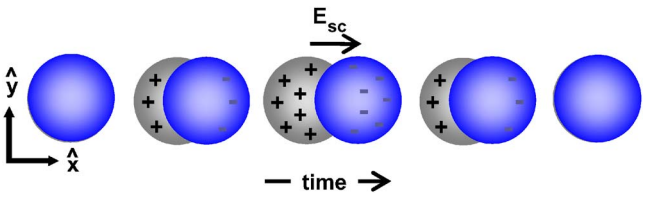

FIG. 3. (Color online) Illustration of the expected relative motion of the electron (−) and hole (+) profiles following their injection with an initial average velocity along the $+x$ and $-x$ directions, respectively. The electron and hole profiles in the x-y plane are shown for several representative times increasing left to right.

broadened by dispersion in the lens to ~200 fs. The transmitted probe pulse is collimated by the pump-focusing lens and detected by one silicon photodiode of a balanced detector, while the reference pulse is directed to the other silicon photodiode. The scattered and reflected pump pulses are blocked using color filters (not shown). The balanced detector produces a signal that is proportional to the difference in the optical powers incident on the two photodiodes. Initially, the powers of the probe and reference beams are adjusted so that the balanced detector produces no output in the absence of pump pulses. In the presence of the pump pulses, the detector produces a signal that is proportional to the change in transmission induced by the pumps. The $\Delta\phi$-*independent* differential transmission $\Delta T(N)/T_0=(T-T_0)/T_0$ (where T and T_0 are the sample transmissions with and without the pumps present) is measured by modulating the pump intensity using a chopper (not shown) and detecting the output of the balanced detector using a lock-in amplifier referenced to the chopping frequency. In contrast, the $\Delta\phi$-*dependent* differential transmission $\Delta T(\Delta\phi)/T(0)=[T(\Delta\phi)-T(0)]/T(0)$ [where now $T(\Delta\phi)$ and $T(0)$ are the sample transmissions at $\Delta\phi$ and $\Delta\phi=0$, respectively] is measured by slaving the lock-in amplifier to the piezoelectric transducer that dithers $\Delta\phi$ about its set value. In this geometry, the signal is enhanced by the tight focusing, and the noise that is common to the two arms of the balanced detectors is suppressed. Spatial resolution is provided by systematically rastering the focused probe across the sample surface [as suggested by the inset in the center of Fig. 2], and temporal resolution is obtained by scanning the time delay τ between the pump pulses and the probe pulse.

These spatially and temporally resolved differential pump-probe measurements are performed with the probe pulse tuned to the heavy-hole excitonic resonance (1.545 eV), and they rely on the well-documented[19–28] changes in the exciton absorption coefficient caused by the presence of free carriers in the valence and conduction bands. In principle, the probe senses the presence of both electrons and heavy holes; however, because the electron effective mass is approximately an order of magnitude smaller than that of the heavy hole, electrons dominate the change in the probe absorption.[19] The light holes (generated by the pump) affect the probe absorption only indirectly through their influence on the heavy-hole distribution function. Since the light-hole mass is much less the heavy-hole mass, there are many fewer light holes than heavy holes, and we neglect the light-hole density. For these reasons, we take the differential transmission to be a measure of electron density only.

In general, the differential transmissions are expected to depend both on the number of electrons in the conduction bands and how they are distributed in energy. However, in the regime where $\Delta T(N)/T_0$ and $\Delta T(\Delta\phi)/T(0)$ are linearly proportional to the electron density N_e and to the change in electron density ΔN_e, respectively, this proportionality allows the density and distribution dependence to be formally separated,

$$\Delta T(N_e)/T_0 = F(t)N_e(x,y,t) \tag{5}$$

and

$$\Delta T(\Delta\phi)/T(0) = F(t)\Delta N_e(\Delta\phi,x,y,t), \tag{6}$$

where $F(t)$ is a function that reflects the identical dependences of $\Delta T(\Delta\phi)/T(0)$ and $\Delta T(N)/T_0$ at a given position and time on the carrier distribution in energy. Once thermalization (but not necessarily cooling) has taken place, this dependence can be described by a carrier temperature T_e (i.e., $F[T_e(t)]$). Since the average excess energy with which each electron is injected into the conduction band is not expected to depend significantly on carrier density or spatial position, neither will T_e $(t=0)$. For a given carrier density, $\Delta T(N)/T_0$ and $\Delta T(\Delta\phi)/T(0)$ [and $F(T_e)$] vary in time as the carriers cool, since electrons located lower in the band are more effective in changing the excitonic absorption. As we discuss below, however, the procedure that we use to isolate the electron transport depends only on the *ratio* $\Delta N_e/N_e = \Delta T(\Delta\phi)/T(0)/\Delta T(N)/T_0$ and, therefore, is insensitive to changes in the electron distribution (e.g., cooling) that do not change the carrier density at that position. This is demonstrated experimentally below.

The procedure for extracting information about the carrier transport at a fixed excitation level and a fixed time delay is illustrated in Fig. 4. For these measurements, the ω and 2ω pump fluences are adjusted so that each pump pulse acting alone produces a peak areal electron density of $\sim 8\times10^{10}$ cm^{-2}, and the time delay between pump probe is set at $\tau=0.42$ ps. Figure 4(a) shows $\Delta T(\Delta\phi,x,y=0,\tau=0.42\text{ ps})/T(0)$ $[\propto\Delta N_e]$ as $\Delta\phi$ is varied at $x=+1.1$ μm (up triangles), 0 μm (open squares), and -1.1 μm (filled circles)]. Several features are worth noting. When $\sin\Delta\phi>0$, the electron density increases on one side of the sample (at $x=+1.1$ μm) and decreases on the other (at $x=-1.1$ μm), consistent with a flow of electrons in the positive direction. When $\sin\Delta\phi<0$, the positions at which the concentration is increased and decreased are reversed. Maxima and minima are observed when $\Delta\phi$ is an odd multiple of $\pi/2$. No increase or decrease in electron density is observed at $x=0$ for any phase. These observations are consistent with Eqs. (3) and (4) and confirm that for parallel polarized ω and 2ω pump pulses QUIC injects a charge current. For the measurements in Fig. 4(b), the phase is fixed at $\Delta\phi=\pi/2$, so that the current is a maximum, and $\Delta T(\Delta\phi)/T(0)$ is measured as a function of position along the x axis $(y=0)$ [filled squares in Fig. 4(b)]. The measured Gaussian profile of the total ($\Delta\phi$-independent) $\Delta T(N)/T_0$ produced by the pumps is also plotted (open circles).

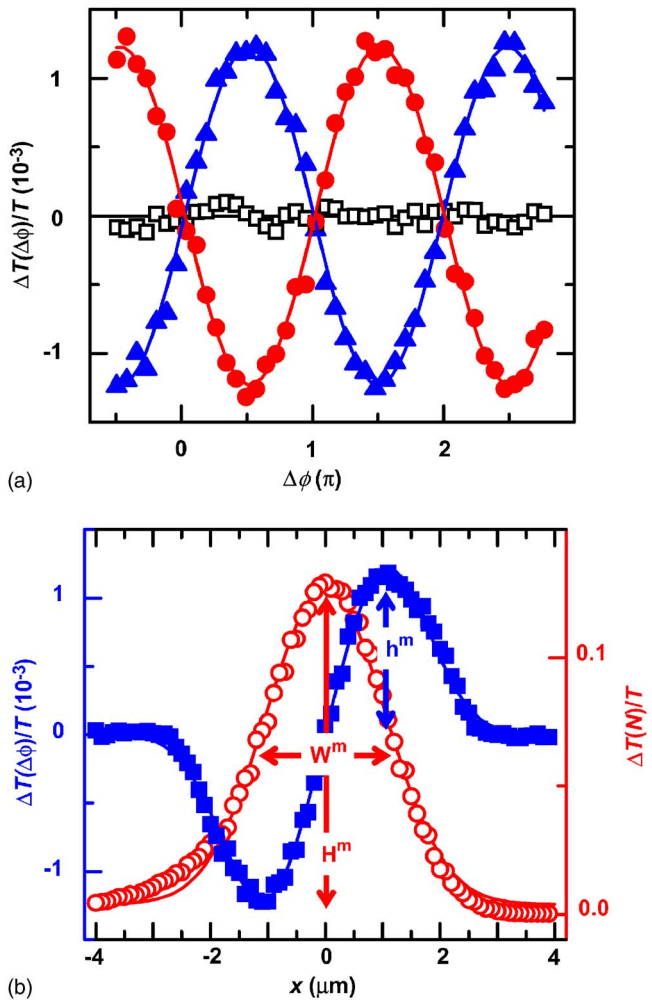

FIG. 4. (Color online) (a) $\Delta T(\Delta\phi)/T(0)$ at a fixed time delay (τ=0.42 ps) and at positions $x=+1.1$ μm (filled up triangles), 0 (open squares), and -1.1 μm (filled circles) as a function of $\Delta\phi$. (b) $\Delta T(\Delta\phi=\pi/2)/T(0)$ (filled squares) and $\Delta T(N)/T_0$ (open circles) as a function of x with $y=0$.

An *average* distance moved per electron x_e in time τ can be extracted from the measurements shown in Fig. 4 by noting that if $x_e \ll W$,

$$\Delta N_e(\Delta\phi,x,y,\tau) = N_e(\Delta\phi,x,y,\tau) - N_e(0,x,y,\tau) \cong -x_e\frac{\partial N_e(0,x,y,\tau)}{\partial x}. \quad (7)$$

For a Gaussian spatial profile, it is straight forward to show that

$$x_e = \frac{1}{2}\sqrt{\frac{e}{2\ln 2}}\frac{\Delta N_0}{N_0}W = \frac{1}{2}\sqrt{\frac{e}{2\ln 2}}\frac{h}{H}W, \quad (8)$$

where $\sqrt{e/(2\ln 2)}/2 \cong 0.7$. The first equality in Eq. (8) states that x_e is found by determining the width W and height N_0 of the Gaussian-shaped carrier distribution N_e and by multiplying the ratio $0.7W/N_0$ by the maximum height ΔN_0 of the derivative ΔN_e produced by that motion [see Fig. 1(a)]. Since $\Delta T(\Delta\phi)/T(0) \propto \Delta N_e$ [see Eq. (6)] and $\Delta T(N)/T(0) \propto N_e$ [see Eq. (5)], $\Delta N_0/N_0 = h/H$, where $h \equiv \Delta T(\Delta\phi=\pi/2)/T(0)$ is the maximum of the derivative-shaped $\Delta T(\Delta\phi)/T(0)$ curve, and H is the maximum height of the Gaussian-shaped $\Delta T(N)/T(0)$ curve. Consequently, the second equality in Eq. (8) indicates that x_e is determined experimentally by measuring the height and width of the $\Delta\phi$-independent differential transmission and the peak of the $\Delta\phi$-dependent differential transmission.

However, H, W, and h are *not* the quantities that are directly measured in our tightly focused experiments. Instead, the $\Delta\phi$-dependent and $\Delta\phi$-independent differential transmissions are measured by using a probe pulse that, by necessity, also has a diameter W, and thus, spatial convolution effects are significant and must be considered. For pulses with Gaussian spatial profiles, it is straightforward to show that the convolution of the probe pulse with $\Delta T(N)/T(0)$ increases the measured width W^m of the spatial profile by $\sqrt{2}$ (i.e., $W^m=\sqrt{2}W$) and decreases the measured height H^m by a factor of 2 (i.e., $H^m=H/2$). By comparison, the convolution of the probe with $\Delta T(\Delta\phi)/T(0)$ reduces the measured peak derivative h^m by $2^{3/2}$ (i.e., $h^m=h/2^{3/2}$). Remarkably, even though the measured height and width of the $\Delta\phi$-independent differential transmission and the peak of the $\Delta\phi$-dependent differential transmission are each significantly changed by the convolution with the probe pulse, the ratio appearing in Eq. (8) is not: $h^mW^m/H^m=hW/H$. Consequently, this procedure for extracting x_e automatically corrects for the probe spatial convolution, and we may use the measured quantities directly.

From Fig. 4(b), x_e=16 nm is extracted using this procedure. It should be emphasized, however, that this is an average (per electron) shift in the position of the electrons at 0.42 ps (relative to their initial position). This technique does not allow us to determine whether a few electrons move much farther than x_e or whether each electron moves exactly this distance. This procedure for extracting x_e also implicitly assumes that diffusion and recombination do not change the electron density profile during our measurements. To confirm that diffusion and recombination make negligible contributions to the carrier dynamics on the time scale of our experiments, we have separately measured the time required for diffusion to double the spatial profile (~200 ps) and the recombination lifetime (~800 ps).

The temporal evolution of x_e at a given excitation level can be obtained by repeating the measurements shown in Fig. 4 as a function of time delay τ and by extracting H^m, W^m, and h^m at each delay. This procedure is illustrated in Fig. 5. H^m initially exhibits a rapid rise as the peak electron density N_0 increases, which follows the integral of the pump pulse envelope and is centered at zero delay. This ~200 fs initial rise is followed by a more gradual increase (~500 fs) that continues after carrier generation is essentially complete and that is consistent with carrier cooling [i.e., an increase in $F(T_e)$ as electrons relax in energy within the conduction band]. Once T_e approaches the lattice temperature and carrier generation is complete, H^m remains constant, indicating a constant N_0 on time scales of a few picoseconds.

By comparison, h^m [solid triangles Fig. 5(a)] exhibits an initial rapid rise followed by a rapid fall back toward zero. The rise is dominated by an increase in the peak derivative like ΔN_0, as the electron profile is shifted by the ballistic

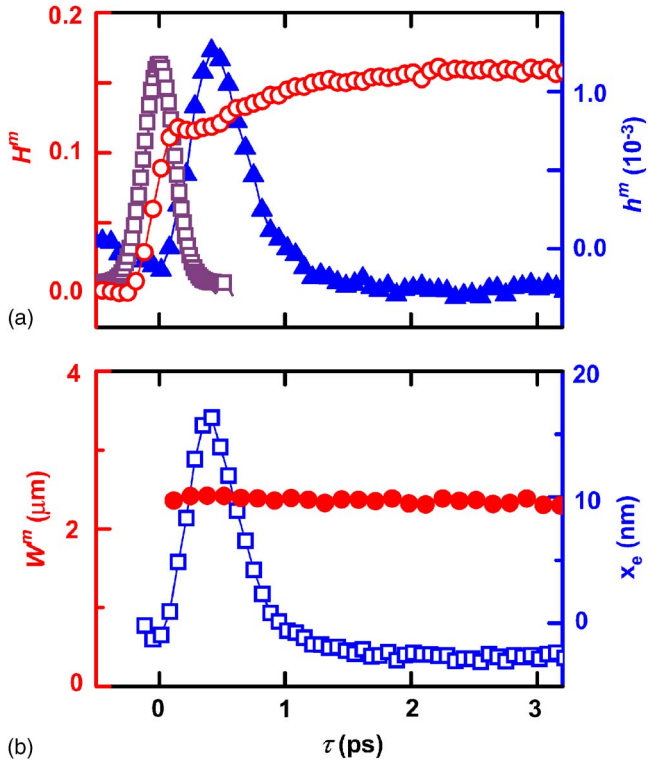

FIG. 5. (Color online) The measured height H^m [open circles in (a)] and width W^m [(solid circles in (b)] of the Gaussian spatial profile of $\Delta T(N)/T_0$ [$\propto N_e$] and the peak height h^m of the derivativelike spatial profile of $\Delta T(\Delta\phi=\pi/2)/T(0)$ [$\propto \Delta N_e$] obtained by repeating the measurements illustrated in Fig. 4 as a function of time delay. The time-dependent average shift of the electrons x_e [open squares in (b)] as extracted from the measurements of H^m, W^m, and h^m. The cross correlation between the ω pump pulse and the probe pulse is shown [open squares in (a)] for comparison.

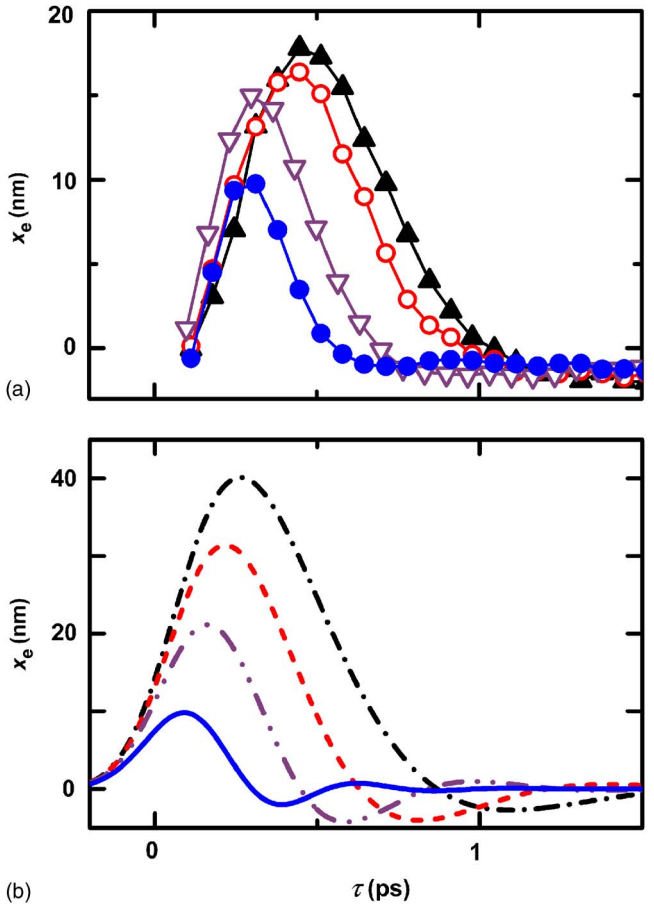

FIG. 6. (Color online) (a) The average distance moved per carrier x_e for injected peak carrier densities of 1.1×10^{11} cm^{-2} (solid up triangles), 1.8×10^{11} cm^{-3} (open circles), 3.4×10^{11} cm^{-3} (open down triangles), and 8.7×10^{11} cm^{-3} (solid circles). (b) x_e predicted by a rigid shift model with no adjustable parameters for the same carrier densities as in (a): 1.1×10^{11} cm^{-3} (dot-dashed lines), 1.8×10^{11} cm^{-3} (dashed lines), 3.4×10^{11} cm^{-3} (dot-dot-dashed lines), and 8.7×10^{11} cm^{-3} (solid lines).

injection current [see Eq. (6)], although the increase in $F(T_e)$ [as T_e decreases] discussed in the previous paragraph also contributes to the initial rise in h^m. The ballistic transport is destroyed by electron-hole and phonon scatterings and the carrier cooling is complete in less than a picosecond. Subsequently, h^m decays as E_{sc} dictates that the electron and hole profiles return roughly to their original positions ($\Delta N_0 \sim 0$). W^m, the measured FWHM of $\Delta T(N)/T_0$ [solid circles in Fig. 5(b)], is constant over the full range shown here and is independent of T_e. Therefore, the temporal evolution of the average distance traveled per carrier x_e extracted using Eq. (8) is independent of the carrier temperature and is shown in Fig. 5(b) (open squares).

The carrier density dependence of x_e is investigated by repeating the measurements described in Figs. 4 and 5 as a function of pump fluence. At each excitation level, the fluences of the ω and 2ω pulses are adjusted so that the carrier density produced by each pulse is approximately the same. Results for selected excitation levels are shown in Fig. 6(a). Both the peak distance moved by the electrons and the time required for them to return to their original positions decrease as the carrier density increases.

IV. RIGID SHIFT MODEL

In order to gain additional insight into the carrier dynamics, a simple "rigid shift" model for the carrier dynamics is considered, wherein it is assumed that the electron or hole profiles do not change shape nor broaden during transport. With this assumption, the evolution of the Gaussian electron N_e and hole N_h profiles can be fully described by tracking the dynamics of the positions of the centers (or peaks) of the electron and hole charge distributions x_e and x_h, respectively,

$$N_{e(h)}(x,y,t) = N_0 \exp\left[-4\ln 2\left(\frac{x-x_{e(h)}(t)}{W}\right)^2\right] \times \exp\left[-4\ln 2\left(\frac{y}{W}\right)^2\right]. \quad (9)$$

Beginning with the hydrodynamic equations for the conservation of mass and momentum, well known arguments[29] can be used to show that the relative coordinate $x_R = x_e - x_h$ obeys the equation

$$\ddot{x}_R = -\Omega^2 x_R - \dot{x}_R/\tau_m, \quad (10)$$

where Ω is the plasma frequency that characterizes the electron-hole spatial distributions and the momentum relaxation time τ_m is given by $1/\tau_m = 1/\tau_{ph} + 2/\tau_{eh}$, where τ_{ph} and τ_{eh} denote the electron-phonon and the electron-hole relaxation times, respectively. In writing Eq. (10), we have as-

sumed that the electron-phonon τ_{ph}^{e} and hole-phonon τ_{ph}^{h} relaxation times are equal: $\tau_{ph}^{e}=\tau_{ph}^{h}=\tau_{ph}$. The plasma frequency Ω for a MQW consisting of N_{QW} quantum wells is given approximately by[29,30]

$$\Omega^2=\frac{1}{4}\sqrt{\pi \ln 2/2}\left[\frac{N_o e^2 N_{\mathrm{QW}}}{\varepsilon m_R^* W}\right], \tag{11}$$

(in MKS units) where the reduced effective mass is given by $1/m_R^*=1/m_e^*+1/m_h^*$ and where we have included an enhancement of ~2 due to space charge effects associated with the semiconductor/air interface.

Ignoring the possibility of a displacement of the center of mass of the electron-hole distributions and assuming that the generation process is instantaneous, the above formulation allows an analytical expression for the average electron displacement,

$$x_e=-\left(\frac{m_h^*}{m_e^*+m_h^*}\right)\frac{\langle v_R(0)\rangle \tau_m \sin(\Delta\phi)}{\sqrt{1-4(\Omega\tau_m)^2}} \times e^{-t/2\tau_m}\left[e^{-\sqrt{1-4(\Omega\tau_m)^2}(t/2\tau_m)}-e^{\sqrt{1-4(\Omega\tau_m)^2}(t/2\tau_m)}\right], \tag{12}$$

where $\langle v_R(0)\rangle=\langle v_e(0)\rangle-\langle v_h(0)\rangle$ is the relative initial average (or swarm) velocity with which the electrons and holes are injected when $\Delta\phi=\pi/2$. Simulations of the dynamics of the center of the electron profile x_e using Eq. (12) for carrier densities corresponding to the data in Fig. 6(a) are shown in Fig. 6(b). For these simulations, no attempt is made to adjust Ω, $\langle v_R(0)\rangle$, or τ_m to fit the data; rather, known parameters for GaAs MQWs are taken from the literature. The plasma frequency is readily calculated from Eq. (11) using parameters independently extracted from the experiments (i.e., N_0 and W). A value of $\langle v_R(0)\rangle=550$ nm/ps (Ref. 29) is used for all simulations; this value depends only on the injection photon energy and is independent of carrier density.

The choice of values to use for τ_m is more difficult. We are unaware of any measurements of the momentum relaxation time τ_m for our experimental conditions. However, Duc *et al.*[31] have performed two-dimensional microscopic quantum-kinetic calculations (based on the semiconductor Bloch equations) of the decay of charge currents injected by quantum interference under conditions appropriate for comparison to our experiments (i.e., at 50 K and $2\hbar\omega-E_g$ ~150 meV)—although the pulse widths (~20 fs) used in their simulations were significantly shorter than those used here, and more importantly, no space charge field effects were included. The latter is advantageous for our purposes since it allows us to extract the momentum relaxation times associated with LO phonon scattering and electron-hole scattering (i.e., Coulomb drag) without the complications of a restoring force. From their figures, we infer values of $\tau_{ph}=$ ~240 fs and $\tau_{eh}/2=$ ~440 fs at an areal density of 10^{11} cm^{-2}. We then make the ansatz that the Coulomb drag contribution to the momentum relaxation time takes the well-known form appropriate for carrier-carrier scattering:[32] $2/\tau_{eh}=cN_e^{1/3}$, where $c=5\times10^{-7}$ cm$^{2/3}$/fs is obtained from a fit to the data from Ref. 31 As expected, these values for the momentum relaxation times τ_m are longer than the corresponding interband dephasing measurements, which have been performed at room temperature in similar MQWs,[32] since electron-electron and hole-hole scatterings contribute to the dephasing of the interband transitions but not to the momentum relaxation. In addition, all of these scattering events are directional to some degree. Thus, a larger number of collisions may be required to randomize the momentum than to destroy the interband coherence.

The simulations shown in Fig. 6(b) qualitatively reproduce the key features of the data. Initially, the electron and hole spatial profiles separate as a result of ballistic transport [i.e., x_e rapidly increases $\propto\langle v_R(0)\rangle t$]. Subsequently, the rate of separation slows as the ballistic charge current is destroyed by momentum relaxation and as the electrons and holes are decelerated by the growing space charge field E_{sc}. The drift associated with E_{sc} eventually causes the electron and hole profiles to return roughly to their original positions. The peak separation decreases and the time required for carriers to return to their original positions decreases as the carrier density increases (i.e., as τ_m decreases and Ω increases). These features are extremely robust and are not sensitive to the values chosen for $\langle v_R(0)\rangle$, Ω, and τ_m, so long as these values are chosen within generally accepted ranges.

We reiterate that the rigid shift model is meant only to illustrate the qualitative features of the ballistic carrier motion. The crudeness of the model does not justify attempts to fit the data and precludes the extraction of experimental parameters, such as τ_m. For example, one of the principal approximations made in deriving Eq. (12) is to replace the Gaussian-shaped E_{sc} associated with the charge distribution ΔN_e represented by Eq. (7) with a spatially independent restoring space charge field. In defining the plasma frequency Ω in Eq. (11), we use the average field $\int\int dxdyE_{\mathrm{sc}}N_e/\int\int dxdyN_e$ for this purpose. In this way, the rigid shift model treats Ω as being independent of spatial coordinates. Similarly, the momentum relaxation time depends on carrier density, and the carrier density varies over the spatial profile. Thus, τ_m also must be viewed as a spatially averaged parameter.

In addition, one might expect the ballistic transport [i.e., $\langle v_R(0)\rangle\tau_m$] associated with the charge current and the drift associated with the space charge field (i.e., Ω) (both of which, in principle, vary in space and time) to lead to a broadening and distortion of the electron and hole spatial profiles. In practice, within experimental error, the carrier profiles remain Gaussian and maintain a constant width in time (e.g., see Fig. 5), and the electron accumulations from the charge currents exhibit well-behaved derivative-like spatial profiles for all excitation levels and all times, giving credence to the rigid shift description.

A more realistic model would incorporate the carrier dynamics in k-space as they thermalize and cool following injection (perhaps an approach similar to Ref. 31), it would include space charge effects, track the carrier motion point by point in real space, and separate coherent and incoherent transports. Finally, such a model would accurately take into account the finite duration of the generation process, and the temporal and spatial convolution effects associated with the probe pulse. [Note that the temporal convolution of the pump pulses with the probe pulse is included in the simulations

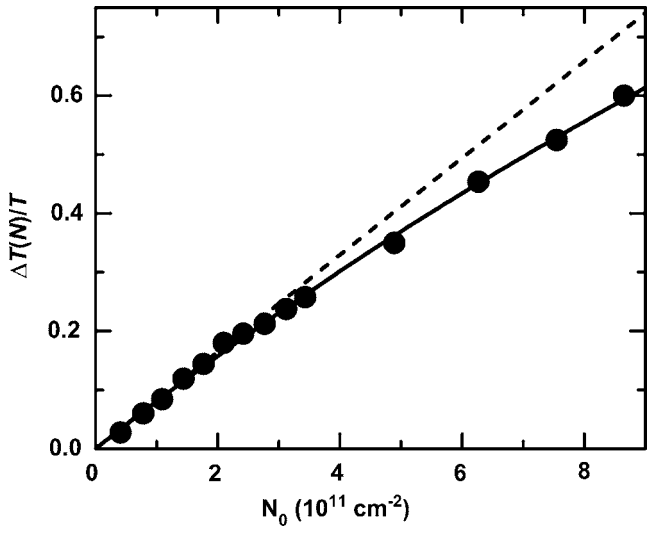

FIG. 7. The measured differential transmission with the probe centered at $x=0$ and $y=0$ and the time delay fixed at $\tau=6$ ps as a function of peak carrier density. The solid line is a fit of the data to Eq. (13) using a saturation density of $N_s=4.3\times10^{12}$ cm^{-3}. The dashed line is the corresponding linear fit (i.e., the $N_s\rightarrow\infty$ limit).

shown in Fig. 6(b), but the nonzero generation time is not.] Such a model is numerically intensive and is beyond the scope of the present paper.

V. NONLINEAR DIFFERENTIAL TRANSMISSION

The technique described in Sec. III for extracting the average distance x_e moved by the electrons following their ballistic injection into the conduction band is based on the assumption that the differential transmission is proportional to the carrier density. In this section, we investigate the validity of that premise for our experimental conditions. Figure 7 shows the differential transmission measured by the probe when it is centered at $x=0$ and $y=0$ as a function of peak carrier density. For these measurements, the time delay is fixed at ~6 ps to ensure that carrrier cooling is complete and that it can be ignored in our present discussions. Clearly, for carrier densities below $\sim3\times10^{11}$ cm^{-2}, the assumption of linearity is a good one; however, above that density, the deviation from linearity is significant. Consequently, the question is how does this nonlinear dependence of $\Delta T(N)/T_0$ on N_e affect the values of x_e extracted using the procedure outlined in Sec. III?

To illustrate the answer to this question, we assume a phenomenological saturation expression for the differential transmission of the probe that is nonlinear in the electron density,

$$\Delta T[N(x,y),\tau]/T_0 \propto N_e(x,y)/[1+N_e(x,y)/N_s], \tag{13}$$

where N_s is a saturation carrier density. The solid line in Fig. 7 is a fit to the data using $N_s=4.3\times10^{12}$ cm^{-3}. Note that N_e is given by Eq. (9) and is produced by absorption of the ω and 2ω pulses, which are tuned high in the bands. Separate measurements of the ω and 2ω transmissivities confirm that they do not measurably saturate at the excitation fluences used here; therefore, the N_e spatial profiles are not distorted by saturation. Rather, it is the transmission of the probe (which is tuned onto the exciton resonance) that is spatially distorted by N_e.

It is straightforward to show that the nonlinear dependence of $\Delta T(N)/T_0$ on N_e given by Eq. (13) leads to a bleaching and broadening of the probe differential transmission profile given by

$$H^s/H = 1/[1+N_e/N_s] \tag{14}$$

and

$$W^s/W = \sqrt{\ln(2+N_e/N_s)}/\sqrt{\ln 2}, \tag{15}$$

respectively. Here, H^s and W^s denote the measured peak height and the width (FWHM), respectively, of the saturated and distorted $\Delta T(N)/T_0$ spatial profile [i.e., Eq. (13)] produced by an electron density N_e. These are normalized by the height H and width W of the undistorted spatial profiles [i.e., Eq. (13) in the $N_s\rightarrow\infty$ limit].

Furthermore, if we assume that the unsaturated, undistorted electron profile N_e is rigidly shifted along the x-axis by a distance x_e [see Eq. (9)], then it is also straightforward to show that

$$h^s/h = (x_p^s/x_p)\sqrt{\pi}\exp[-4\ln 2(x_p^s/W)^2]/\{1+(N_e/N_s) \times\exp[-4\ln 2(x_p^s/W)^2]\}^2, \tag{16}$$

where h^s is the measured derivative-like peak in the saturated phase-dependent differential transmission $\Delta T(\Delta\phi)/T(0)$ of the probe and h is the actual peak of the derivative in the absence of saturation. h^s occurs at the inflection point of the distorted $\Delta T(N)/T_0$ profile, and its location x_p^s can be found by numerically solving the following transcendental equation:

$$(x_p^s/x_p)^2 = \{1+(N_e/N_s)\exp[-4\ln 2(x_p^s/W)^2]\}/\{1 - (N_e/N_s)\exp[-4\ln 2(x_p^s/W)^2]\}, \tag{17}$$

where $x_p=W/(2\sqrt{2\ln 2})$ gives the position of the inflection point for the Gaussian profile in the absence of saturation.

The height H^s and width W^s of the saturated differential transmission spatial profile and the peak in the derivative h^s produced by a rigid shift of the electron density profile N_e by a distance x_e are shown as a function of the fractional peak saturation carrier density N_0/N_s in Fig. 8. The shift $x_e^s=0.7h^sW^s/H^s$ [normalized by the actual shift $x_e=0.7hW/H$, see Eq. (8)], which would be extracted if one blindly used these saturated parameters, is also shown for comparison.

Figure 8 clearly illustrates the remarkable insensitivity of the procedure for extracting the average electron shift to saturation effects. Over the range shown, H^s and h^s decrease by >30%, and W^s increases by ~15%; however, since x_e^s is determined from the ratio h^sW^s/H^s, these distortions tend to cancel. The net result is that x_e^s/x_e changes by <10%. From Fig. 7, we estimate the range for our experiments to be $N_0/N_s<0.25$. Consequently, errors in our experiments associated with a nonlinear dependence of the differential transmission on N_e are estimated to be <5%.

It should be noted that the insensitivity of our technique to nonlinear saturation effects, which is illustrated here, is robust and not dependent on the particular model taken for the saturation [i.e., on the functional form of Eq. (13)]. This

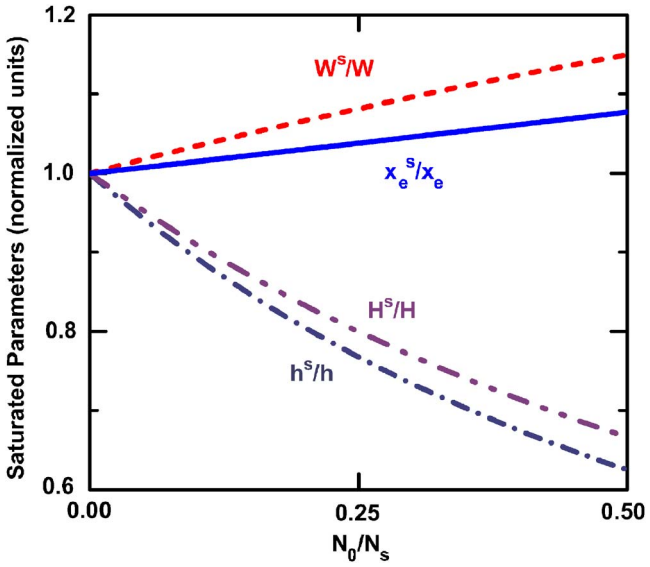

FIG. 8. (Color online) The calculated height H^s and width W^s of the saturated differential transmission spatial profile of the probe, $\Delta T(N(x,y),\tau)/T_0$, represented by Eq. (13), and the peak height of the derivative h^s, produced by a rigid shift of the electron density profile N_e by a distance x_e as a function of N_0/N_s. H^s, W^s, and h^s are normalized by the corresponding values (H, W, and h) that would be obtained in the absence of nonlinear saturation (i.e., the values when $N_s \to \infty$). $x_e^s = 0.7h^s W^s/H^s$ is the shift that would be extracted using the distorted (non-Gaussian) profile and $x_e = 0.7hW/H$ is the shift extracted using the undistorted profile.

is not surprising since any saturation that increases nonlinearly with carrier density will intrinsically decrease both h and H, making the ratio h/H less sensitive to these changes, while increasing W.

VI. SUMMARY

By using collinearly incident 1430 and 715 nm, 200 fs tightly focused and overlapping pulses, in a GaAs/AlGaAs MQW, we are able to inject charge currents whose spatial and temporal evolutions are monitored through the differential transmission of a probe beam tuned to the exciton resonance. From these experiments, we obtain quantitative information on the average distance that the electrons move as a function of time and obtain qualitative information on the ballistic transport that leads to the formation of space charge fields which oppose the charge motion and on the momentum relaxation processes that destroy the ballistic transport. The procedure for extracting the electron motion is shown to be unaffected by the relaxation dynamics of the hot electrons and the spatial convolution of pumps and probe and to be forgiving of nonlinear saturation effects. The results are analyzed in terms of a simple rigid shift (simple harmonic oscillator) model, which is able to reproduce the main features of the data.

ACKNOWLEDGMENTS

The authors thank Rashad Abrarov, Ali Najmaie, Eugene Sherman, and John Sipe for many insightful discussions. This work was supported by the Office of Naval Research and NSERC.

[1]For recent reviews, see, for example, H. M. van Driel and J. E. Sipe, in *Ultrafast Phenomena in Semiconductors*, edited by K.-T. Tsen (Springer, New York, 1999); M. J. Stevens, R. D. R. Bhat, A. Najmaie, H. M. van Driel, J. E. Sipe, and A. L. Smirl, in *Optics of Semiconductors and Their Nanostructures*, Springer Series in Solid-State Science Vol. 146, edited by H. Kalt and M. Hetterich (Springer-Verlag, Berlin, 2004).
[2]R. Atanasov, A. Hache, J. L. P. Hughes, H. M. van Driel, and J. E. Sipe, Phys. Rev. Lett. **76**, 1703 (1995).
[3]A. Hache, Y. Kostoulas, R. Atanasov, J. L. P. Hughes, J. E. Sipe, and H. M. van Driel, Phys. Rev. Lett. **78**, 306 (1997).
[4]T. M. Fortier, P. A. Roos, D. J. Jones, S. T. Cundiff, R. D. R. Bhat, and J. E. Sipe, Phys. Rev. Lett. **92**, 147403 (2004).
[5]P. A. Roos, X. Li, R. P. Smith, J. A. Pipis, T. M. Fortier, and S. T. Cundiff, Opt. Lett. **30**, 735 (2005).
[6]D. Cote, J. M. Fraser, M. DeCamp, P. H. Bucksbaum, and H. M. van Driel, Appl. Phys. Lett. **75**, 3959 (1999).
[7]M. J. Stevens, A. Najmaie, R. D. R. Bhat, J. E. Sipe, H. M. van Driel, and A. L. Smirl, J. Appl. Phys. **94**, 4999 (2003).
[8]W. Z. Lin, Q. Shou, L. N. Liu, Y. Wu, J. H. Wen, and T. S. Lai, Chin. Phys. Lett. **22**, 188 (2004).
[9]H. Zhao, E. J. Loren, H. M. van Driel, and A. L. Smirl, Phys. Rev. Lett. **96**, 246601 (2006).
[10]R. D. R. Bhat and J. E. Sipe, Phys. Rev. Lett. **85**, 5432 (2000).
[11]M. J. Stevens, A. L. Smirl, R. D. R. Bhat, A. Najmaie, J. E. Sipe, and H. M. van Driel, Phys. Rev. Lett. **90**, 136603 (2003).
[12]J. Hübner, W. W. Rühle, M. Klude, D. Hommel, R. D. R. Bhat, J. E. Sipe, and H. M. van Driel, Phys. Rev. Lett. **90**, 216601 (2003).
[13]M. J. Stevens, A. L. Smirl, R. D. R. Bhat, J. E. Sipe, and H. M. van Driel, J. Appl. Phys. **91**, 4382 (2002).
[14]H. Zhao, A. L. Smirl, and H. M. van Driel, Phys. Rev. B **75**, 075305 (2007).
[15]Y. Kerachian, P. A. Marsden, H. M. van Driel, and A. L. Smirl, Phys. Rev. B **75**, 125205 (2007).
[16]R. D. R. Bhat and J. E. Sipe, e-print arXiv:cond-mat/0601277.
[17]A. Najmaie, R. D. R. Bhat, and J. E. Sipe, Phys. Rev. B **68**, 165348 (2003).
[18]A. Hache, J. E. Sipe, and H. M. van Driel, IEEE J. Quantum Electron. **34**, 1144 (1998).
[19]S. Schmitt-Rink, D. S. Chemla, and D. A. B. Miller, Phys. Rev. B **32**, 6601 (1985).
[20]R. Zimmermann, Phys. Status Solidi B **146**, 371 (1988).
[21]T. Meier and S. W. Koch, Phys. Rev. B **59**, 13202 (1999).
[22]A. Thilagam, Phys. Rev. B **59**, 3027 (1999).
[23]K. C. Je, M. Choi, S. Y. Yim, J. S. Ahm, and S. H. Park, Phys. Rev. B **66**, 155312 (2002).
[24]M. Wegener, I. Bar-Joseph, G. Sucha, M. N. Islam, N. Sauer, T. Y. Chang, and D. S. Chemla, Phys. Rev. B **39**, 12794 (1989).
[25]P. C. Becker, D. Lee, A. M. Johnson, A. G. Prosser, R. D. Feldman, R. F. Austin, and R. E. Behringer, Phys. Rev. Lett. **68**, 1876 (1992).
[26]W. H. Knox, C. Hirlimann, D. A. B. Miller, J. Shah, D. S. Chemla, and C. V. Shank, Phys. Rev. Lett. **56**, 1191 (1986).
[27]S. Hunsche, K. Leo, H. Kurz, and K. Köhler, Phys. Rev. B **49**, 16565 (1994).
[28]D. Huang, J. I. Chyi, and H. Morkoç, Phys. Rev. B **42**, 5147 (1990).
[29]E. Ya. Sherman, A. Najmaie, H. M. van Driel, A. L. Smirl, and J. E. Sipe, Solid State Commun. **139**, 439 (2006).
[30]T. Ando, A. B. Fowler, and F. Stern, Rev. Mod. Phys. **54**, 437 (1982).
[31]H. T. Duc, T. Meier, and S. W. Koch, Phys. Rev. Lett. **95**, 086606 (2005).
[32]W. A. Hügel, M. F. Heinrich, M. Wegener, Q. T. Vu, L. Bányai, and H. Haug, Phys. Rev. Lett. **83**, 3313 (1999).